Available online at www.sciencedirect.com

ScienceDirect

journal homepage: www.elsevier.com/locate/he

Electrochemical hydrogen storage in high surface area microporous carbon from disposable diaper waste

César Giovanni-Mondragón [a], Diego Ramón Lobato-Peralta [a], Jude A. Okolie [b], D.M. Arias [a], Henry O. Orugba [c], P.J. Sebastian [a], Patrick U. Okoye [a,*]

[a] Instituto de Energías Renovables (IER-UNAM), Privada Xochicalco s/n Col. Centro. Temixco, Morelos, 62580, Mexico

[b] Gallogly College of Engineering, University of Oklahoma, Norman, OK, 73019, USA

[c] Department of Chemical Engineering, Delta State University, Abraka, Nigeria

HIGHLIGHTS

- Diaper waste was used as a sustainable precursor to prepare activated carbon.
- Abundant micropores and high surface area allowed high hydrogen storage capacity.
- Higher current density achieved faster release of adsorbed hydrogen atoms.
- The mechanism of hydrogen storage is mainly electric double layer.

ARTICLE INFO

Article history:
Received 7 August 2023
Received in revised form
20 September 2023
Accepted 22 September 2023
Available online 07 October 2023

Keywords:
Hydrogen
Microporosity
Statistical analysis
Activated carbon
Energy storage

ABSTRACT

The superabsorbent polymer (SAP) of the disposable diaper, which could serve as a substrate for pathogen growth, was valorized into nanostructured carbon through chemical activation for electrochemical hydrogen storage. The Box-Behnken experimental design was employed to elucidate the effects of activation conditions. Optimization results show that activation temperature and KOH:SAPC molar ratio had a greater impact on the textural and morphological characteristics of the nano-activated carbon. The best electrode material exhibited a surface area of 2552 m^2/g, a total pore volume of 1.28 cm^3/g, a total micropore volume of 0.871 cm^3/g, and a pore size of 1.32 nm. The galvanostatic charge/discharge curves indicate that only higher current densities of 1 and 2 A/g could achieve a faster release of stored hydrogen in approximately 4 min. The best material stored hydrogen mainly through the electric double-layer mechanism, and the specific capacity reached 1878 mAh/g (6.60 wt% of H_2), which ranks among the best-reported hydrogen storage capacities with activated carbon.

* *Corresponding author.*
E-mail address: ugopaok@ier.unam.mx (P.U. Okoye).

https://doi.org/10.1016/j.ijhydene.2023.09.239

1. Introduction

Generally, hydrogen, especially from renewable sources, is regarded as a pollution-free energy resource that could diminish the demand for fossil fuels and mitigate greenhouse gases. However, there are several issues not only with the production of hydrogen but also with its applications and storage [1]. Critical issues related to hydrogen storage include safety, capacity in terms of volumetric and gravimetric storage capacity, and ease of reversibility [2]. Hence, researchers have made efforts to address these challenges.

Concerning safety issues, some researchers have turned to underground hydrogen storage in salt aquifers or depleted gas reservoirs. Electrochemical adsorption of hydrogen using transition metals and metal alloys has been widely implemented under ambient conditions, demonstrating remarkable storage capacity [3–5]. These metals include metal hydrides, borohydrides, and chemical hydrides; however, these metals are expensive, require complex and energy-intensive synthesis routes, and are relatively heavy [6]. Additionally, materials such as strontium chromate-nitrogen and sulfur co-doped graphene [7], Mo_2C/Co_9S_8/N-doped carbon [8], graphene oxide [9], metal-organic UiO-66 framework/graphene composites [10], and ammonium uranate/graphene [11] nanocomposites have been employed to electrochemically store a significant amount of hydrogen.

An alternative to these metal hydrides is carbon materials, which are lightweight and possess appreciably high electronic conductivity, as well as offering low cost and a large surface area, which enables enhanced interaction between its surface and hydrogen for adsorption [12]. These carbon materials, when used as cathodic polarized electrodes, can store atomic hydrogen in their pores and interlayers when in contact with an aqueous electrolyte [13–15]. The challenges of hydrogen storage in carbon have been well-documented. This is because the interaction force between carbon and hydrogen is usually unsuitable for retaining and releasing hydrogen under the operating conditions of an ideal fuel cell. Additionally, the sp^2 hybridization configuration of most activated carbon allows a carbon atom to bind to three neighboring atoms through s or π bonds [16]. This type of bonding typically involves weak van der Waals forces, which are insufficient for retaining hydrogen molecules under room temperature and pressure. On the other hand, atomic hydrogen storage could lead to a shift from sp^2 to sp^3 hybridization, resulting in stronger chemical bonding that would require heating to release the stored hydrogen [17,18]. Implementing this scenario in many devices would be a challenging task. Therefore, the research problem is to fine-tune the carbon-hydrogen interaction so that its magnitude falls between chemisorption and physisorption.

Some researchers have utilized activated carbon for electrochemical hydrogen storage [19–22]. In many cases, activated carbon is functionalized with transition or noble metals to enhance the activation of hydrogen atoms in the aqueous electrolyte. For instance, Akbarzadeh et al. [23] developed a composite material consisting of Fe–Ag/TiO_2/CNT electrodes for electrochemical hydrogen storage under ambient conditions. They observed that this material exhibited a remarkable improvement in hydrogen accumulation within its pores. This enhancement was attributed to the excellent redox capability of TiO_2, which facilitated enhanced interfacial diffusion of hydrogen. The performance of this material exceeded that of unmodified multi-walled carbon nanotubes, with a hydrogen storage capacity of approximately 10.94 wt% compared to 2.19 wt% in the unmodified nanotubes. Furthermore, it demonstrated a high and stable discharge capacity even after 20 cycles, making it a promising candidate for battery applications. Similarly, Sedighi et al. [3] employed a ternary composite electrocatalyst comprising $Ce_2W_2O_9/CoWO_4$/porous carbon for hydrogen storage. This nanocomposite was synthesized through an emulsion-assisted sonochemical reaction, followed by thermal treatment. It exhibited the ability to store hydrogen via the Tafel and Heyrovsky mechanisms, achieving an impressive hydrogen storage capacity of about 660 mAh/g.

Activated carbon derived from walnut shells deposited on copper foam has been employed for electrochemical hydrogen storage [24]. Interestingly, the presence of copper foam was found to have a negligible impact on hydrogen storage. Despite the mesoporous nature of their carbon material, the researchers argued that the crucial factors affecting activated carbon's suitability for hydrogen storage are not solely pore size, but also surface area, carbon curvature, and the pore size relative to the adsorbate molecule. They achieved an impressive hydrogen storage capacity of 5.66 wt%. In another study, the carbon-hydrogen interaction mechanism was evaluated using activated carbon derived from phenolic resin [12]. X-ray photoelectron spectroscopy (XPS) analysis revealed a 61% sp^2 hybridization fraction in the C–H interaction. Hydrogen storage capacity was assessed through discharge cycles using a proton battery. Raman spectra indicated the presence of 33% graphitic carbon with a sp^3 fraction of 32.29%. The primary storage mechanism involved an electric double layer (EDLC), resulting in a hydrogen storage capacity of only 0.65 wt%.

Diaper waste is an abundant material typically destined for landfill disposal. A diaper consists of approximately 33% sodium polyacrylate (a superabsorbent polymer, SAP), 35% cellulose pulp, 17% polypropylene, adhesives, and other components [25,26]. SAP, known for its high-density polymer structure, is responsible for absorbing and retaining urine. However, this superabsorbent polymer decomposes slowly, and due to its contact with urine and feces, it can serve as a breeding site for pathogens [27]. Therefore, its transformation into porous carbon presents a viable strategy to reduce waste, generate value-added materials, and promote environmental cleanliness. In this study, we employed SAP extracted from disposable diapers to produce high-surface-area activated carbon. We conducted an analysis of the physicochemical properties of the resulting carbon to elucidate its textural and surface characteristics, which are relevant to the hydrogen storage mechanism.

2. Experimental

2.1. Activated carbon production

The diaper waste was washed with deionized water and then dried under solar irradiation for 48 h. The superabsorbent

polymer (SAP) was manually extracted and torn into smaller pieces. It was subsequently ball-milled for 30 min. The resulting ball-milled sample was placed in a 20 mL alumina crucible and subjected to carbonization in a Linderberg Blue M furnace, equipped with a tubular stainless-steel reactor, at 500 °C. The heating rate was set at 20 °C/min, and the process lasted for 90 min under a nitrogen flow of 100 mL/min. Following carbonization, the sample was ground into a powder and then activated using KOH. The sample obtained after carbonization is referred to as superabsorbent polymer carbonized (SAPC). For experimental design and the investigation of the KOH:SAPC molar ratio, temperature, and time's impact on the activated carbon's characteristics, we adopted the Box-Behnken design. These values were chosen based on prior research and experience in carbon materials synthesis. Table 1 displays the design matrix, and Table 2 indicates the total number of experimental runs, which is 15.

Table 1 – Coded values and limits of the factors.

Factors	Unit	Coded values		
		− 1	0	+1
A: Temperature	°C	700	800	900
B: Time	h	1	1.5	2
C: KOH:SAPC	wt/wt	1	2.5	4

Table 2 – The experimental design table.

Sample (R)	A: Temperature (°C)	B: Time (h)	C: KOH: SAPC (wt/wt)
1	700	2	2.5
2	900	1	2.5
3	700	1.5	1
4	800	1.5	2.5
5	800	2	1
6	800	1	4
7	900	1.5	1
8	700	1.5	4
9	700	1	2.5
10	800	1	1
11	900	1.5	4
12	800	2	4
13	900	2	2.5
14	800	1.5	2.5
15	800	1.5	2.5

2.2. Characterization of the materials

To quantify the surface area, we employed nitrogen physisorption at 77 K, utilizing a Nova 2200e Quantachrome apparatus equipped with NovaWin software. The surface area of the material was determined through Brunauer-Emmett-Teller analysis (BET) and the quenched solid density functional theory (QS-DFT) method [28]. The pore size and pore distribution were assessed using the QS density functional theory (QS-DFT) method.

Powder X-ray diffraction (XRD) measurements were employed for phase identification and to determine the graphitization of the resulting carbon [29]. The XRD diffractometer used was the Rigaku UltimaIV, operating with CuKα radiation at a voltage of 40 kV and a current of 30 mA. The sample was scanned within a 2θ range of 10–70°.

Fourier transform infrared (FTIR) spectroscopy was employed to assess the surface functional groups. Infrared spectra were recorded within the wavenumber range of 500–4000 cm^{-1} using a Brucker Tensor 27 instrument. Sample preparation was conducted following the KBr pellet technique.

Sample morphologies were examined using the Hitachi S5500 field emission scanning electron microscope (FE-SEM). Images were captured at various magnifications, including × 5000 and × 15,000. The elemental composition was determined through energy dispersive spectroscopy, which was integrated with the FE-SEM.

2.3. Electrochemical test

All the electrochemical tests were performed in a VMP-300 potentiostat (Biologic) at a room temperature that corresponded to 298 K. For this purpose, 3-electrode cell test systems were assembled with the obtained activated carbons as working electrodes, a graphite rod as counter electrode and Ag/AgCl as reference. The electrolyte for all the experiments corresponded to 6 M KOH. The followed methodology to prepare the working electrodes is explained in the following subsection.

2.3.1. Fabrication of electrode

Carbon electrodes were prepared using activated carbon, commercial conductive carbon (also known as carbon black, Super P Li from Timcal), and polytetrafluoroethylene (PTFE from Sigma Aldrich) as the binder. The binder, carbon black, and activated carbon were weighed in a ratio of 1:1:8. They were then dissolved and stirred in 10 mL of ethanol at 60 °C until a moldable paste was formed. Subsequently, this paste was evenly spread onto a stainless-steel mesh with a geometric area of 1 cm^2 and dried in the furnace at 80 °C overnight. It was then pressed with a force of 7 tons. The material underwent a cleaning process to remove carbon that was not strongly adhered to the steel mesh. For active mass and weight calculations, please refer to Table S1 (the supplementary file is available in the electronic copy).

2.3.2. Galvanostatic charge/discharge test

Galvanostatic charge and discharge tests (GCD), also known as Constant Current Charge and Discharge tests, are employed to assess energy storage systems and materials. This technique entails applying constant positive and negative currents to charge and discharge a material or system while maintaining a predetermined potential limit. The GCD profiles obtained were utilized to analyze the capacitive response quality and Faradaic reactions [30]. GCD tests were conducted at specific currents of 2, 1, 0.5, and 0.2 A/g, and the specific capacitance can be determined from the discharge using Eq. (1) [31].

$$C_{GCD} = \frac{I^{*}t}{m\Delta V} \quad (1)$$

where I(A) is the applied current, ΔV is the potential window (V), t(s) corresponds to the GCD discharge time, m is

the active mass (in this case 80% of the total weight of the electrode mass) and C_{GCD} is the GCD specific capacitance in F/g.

2.3.3. Cyclic voltammetry

Cyclic voltammetry (CV) was employed to characterize the electrochemical performance and elucidate the reaction mechanism [32]. CV tests were conducted at various voltage scan rates ranging from 20 mV/s to 500 mV/s. The voltammogram profiles were analyzed to gain insights into the redox reactions, mass transport, and reactivity properties of the 6 M KOH electrolyte. It is worth noting that the applied electrical potential at the electrode/electrolyte interface varies linearly with time during the potential sweep [33]. The area beneath the rectangular CV curve was determined and integrated. Importantly, the specific capacitance obtained from CV and GCD tests could be closely related at the same scan rate. The integration was performed using the fully licensed edition of OriginLab Pro 2022.

2.3.4. Hydrogen uptake

Hydrogen adsorption on the carbon electrode was calculated according to Eq. (2) [34]:

$$H = H_C - \frac{C}{970} \tag{2}$$

where $H_c = Q/270$, and substituting this term into the formula above, gives Eq. (3).

$$H = \frac{Q}{270} - \frac{C^*\Delta V}{970} \tag{3}$$

where, H_c is the total hydrogen sorption capacity, which is calculated from the Q, that is, the charge during the electrode discharge at the galvanostatic test divided by 270 assuming using Faraday's law that 1 wt% of the adsorbed hydrogen corresponds to this charge (270 mAh/g). C is the specific capacitance of the activated carbon electrodes obtained from the CV curves, considering the area inside of the 200 mV/s curve and ΔV is the potential window used that is from −1 to 0 V, which means a range of 1 V.

3. Results and discussion

3.1. Nitrogen physisorption analysis

Nitrogen physisorption experiments were conducted on some of the samples to investigate their textural characteristics. Specifically, the samples with the highest and lowest hydrogen storage capacities were examined. Fig. 1a displays the sample (R9) with the highest hydrogen storage, while Fig. 1b (R11) represents the one with the lowest hydrogen storage. It is evident that R9 exhibited a combination of type I and type IV adsorption/desorption isotherms with H2 hysteresis [35]. The type I isotherm is noticeable with a knee curve at a lower relative pressure, transitioning abruptly to type IV at higher relative pressures with hysteresis. The presence of type I isotherms suggests the existence of micropores, while the appearance of type IV isotherms and hysteresis are indicative of mesopores with an irregular distribution. The coexistence of these pore types, along with the substantial nitrogen uptake even at lower relative pressures, suggests a significant micropore volume [36]. As shown in Table 3, R9 has an impressively high surface area of 2555 m^2/g, a total pore volume of 1.29 cm^3/g, and a substantial micropore volume of 0.880 cm^3/g when compared to R2. These characteristics notably contribute to its high hydrogen uptake capacity. Conversely, the significantly lower hydrogen uptake observed in R11 is attributed to its reduced surface area, lower micropore volume, and larger pore size. The adsorption isotherm and hysteresis of R11 are similar in type to those of R9. However, the y-axis of R11 indicates that the magnitude of nitrogen adsorption is considerably lower than that of R9. These findings align with previous reports highlighting the critical influence of pore distribution, microporosity, and high surface area on hydrogen storage capacity [37].

3.2. X-ray diffraction analysis of the activated carbon

X-ray diffraction analysis (Fig. 2) was employed to determine the crystallinity of the carbon materials and the changes that occur between the sample that has only been carbonized (SAP

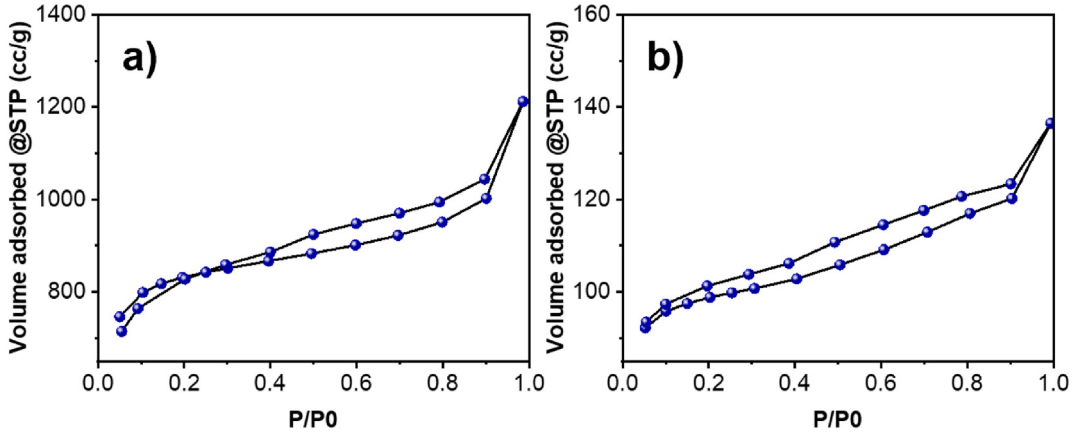

Fig. 1 – Nitrogen physisorption isotherms (a) R9 with highest hydrogen storage capacity and (b) R11 with lowest storage capacity.

Table 3 – Specific surface area of selected activated carbons.

Sample	BET surface area (m^2/g)	Total pore volume (cm^3/g)	Micropore volume (cm^3/g)	Mesopore volume (cm^3/g)	Average pore size (nm)	Storage capacity (wt%)
R9	2555	1.29	0.880	0.448	1.30	6.604
R2	2258	1.23	0.869	0.436	1.39	5.784
R11	298	0.26	0.189	0.165	3.94	1.398

carbon) and the activated samples, using R9 as example. The carbonized sample (SAP carbon) exhibits various diffraction peaks, corresponding to trona ($Na_3H(CO_3)_2 \cdot H_2O$), cristobalite (SiO_2), nahcolite ($NaHCO_3$), thermonatrite ($Na_2CO_3 \cdot H_2O$). As can be observed, the majority of these compounds are sodium-based, which is a significant component in the superabsorbent polymer, as mentioned in the introduction section. The presence of amorphous carbon was confirmed in the best-performing material with the highest storage capacity (R9). The activated carbon exhibited a peak within the 2θ range of 25°–35°, corresponding to the (0 0 2) plane, which confirms the amorphous nature of the material [38,39]. Additionally, a shoulder peak at around 44°, corresponding to the (1 0 1) plane, was observed, suggesting the formation of condensed graphite [40]. The X-ray diffraction pattern did not visibly show peaks due to inorganic elements, which can be attributed to their removal during the impregnation process with KOH and subsequent activation. It is worth mentioning that activation temperature from 500 to 900 °C allows for the obtaining of amorphous carbon and above this temperature range, hard carbon with reduced surface area and porosity is generated.

3.3. *Scanning electron microscope and electron dispersive x-ray (EDS)*

The SEM analysis is depicted in Fig. 3. The raw SAP (Fig. 3a) appears as a dense, high-molecular-weight polymer without porosity but exhibits minor cracks and slits. The whitish deposits observed on the SAP materials are attributable to the presence of inorganic elements within the material. Following carbonization (Fig. 3b), a limited number of pores, along with cracks, slits, and a rod-like morphology, can be observed. Upon activation, the sample with the lowest hydrogen uptake displays a foam-like morphology (Fig. 3c) with white deposits, which may consist of inorganic elements, as confirmed by EDS analysis. Conversely, the samples with the highest hydrogen uptake exhibit a greater degree of porosity and a disordered morphology characteristic of activated carbon (Fig. 3d). Furthermore, the honeycomb-like morphology observed in the R9 sample indicates interconnected pores, which facilitate mass transport and hydrogen storage.

The EDS data presented in Table 4 provides the elemental composition of the raw, carbonized, and activated samples. The raw SAP samples contained carbon, oxygen, silica, and

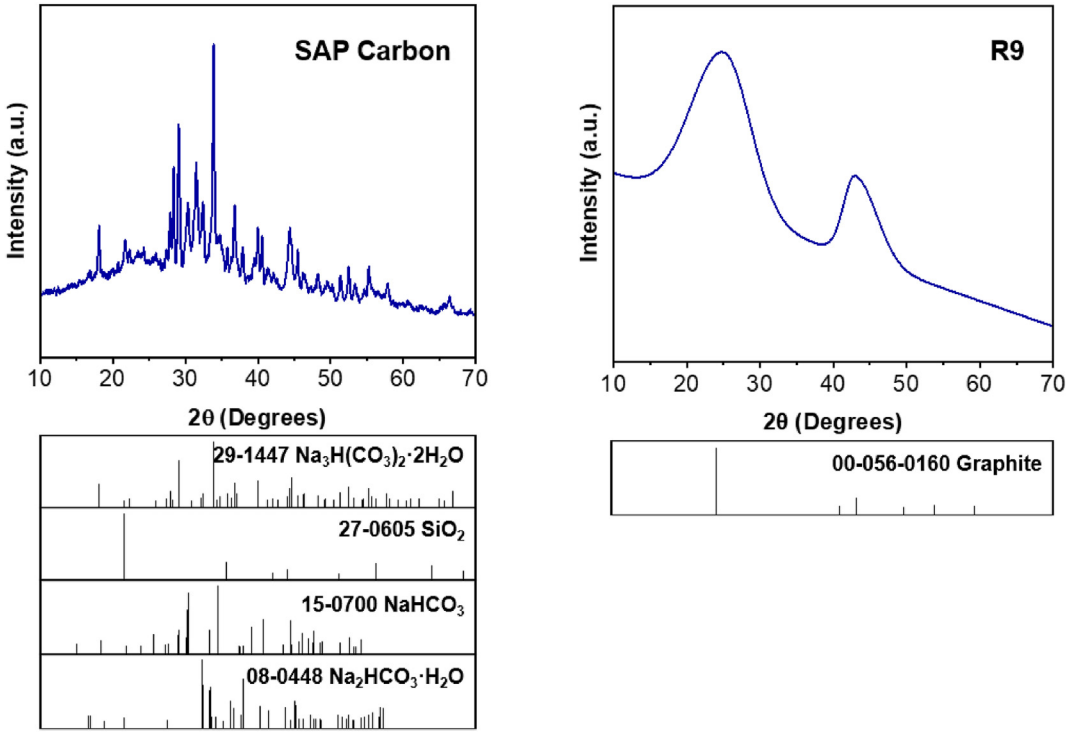

Fig. 2 – XRD spectra of SAP carbon and R9 sample.

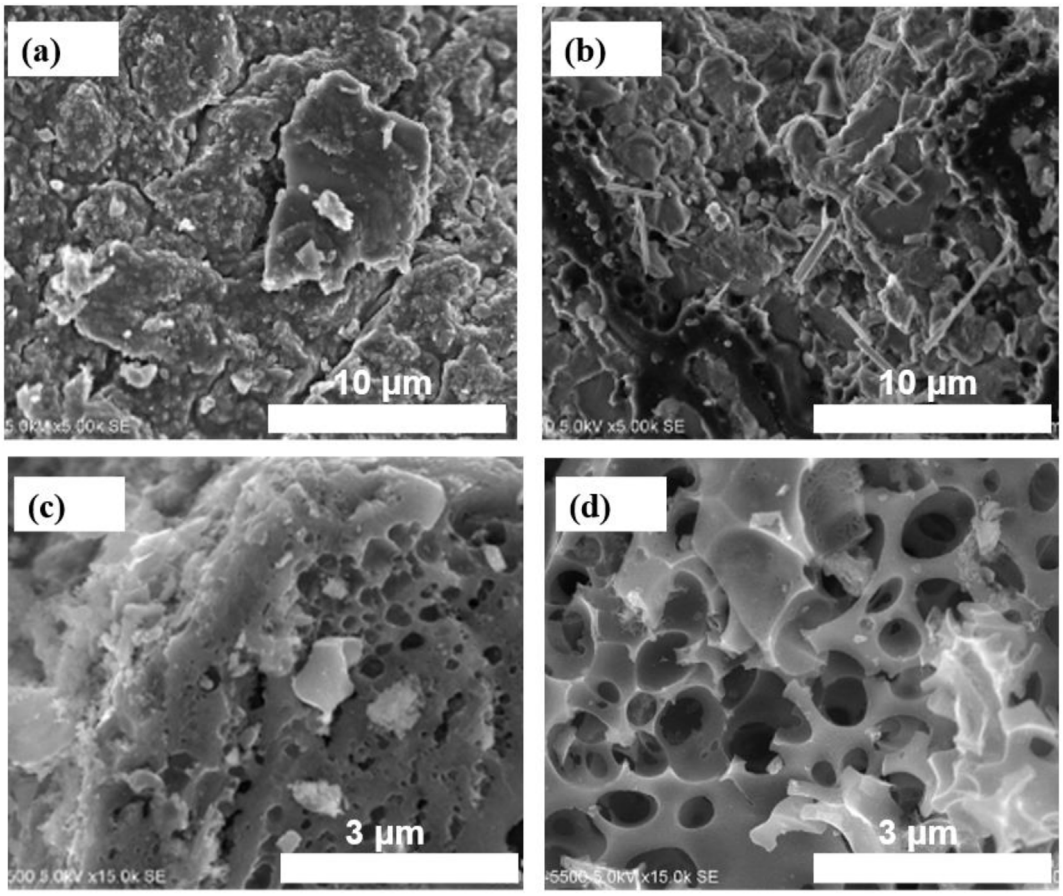

Fig. 3 – SEM images of samples (a) raw SAP, (b) carbonized SAP, (c) R11, (d) R9.

notably, a high concentration of sodium and potassium, likely originating from urine content. Following carbonization, some of these compounds underwent decomposition. During activation, particularly sodium and phosphorus, these elements further decomposed. It is worth mentioning that these elements may contribute to pore formation as they are released as gases. Interestingly, elemental nitrogen was observed after activation, which can be attributed to the nitrogen gas atmosphere used in the activation process. Importantly, heteroatoms like nitrogen can enhance hydrogen sorption by modifying the carbon binding energy [1], while silica and aluminum may assist in hard templating for pore formation [41]. Although there was not a significant difference in the carbon content between R9 and R11, their adsorption capacities differed significantly. One possible explanation could be a substantial reduction in the size and number of pores, as observed in SEM images, resulting in a predominantly rigid carbon structure in one of the samples.

3.4. *Fourier transform infrared analysis*

The sample exhibits a small peak at approximately 1720 cm^{-1}, which can be attributed to carboxylic acid (COOH) groups (Fig. 4). Similarly, peaks are observed around 600 cm^{-1} and 1150 cm^{-1}. According to Ref. [42], peaks below 1000 cm^{-1} are associated with C–H out-of-plane vibrations, corresponding to the bending of benzene and its derivatives. Peaks falling in the range of 1000–1300 cm^{-1} are related to C–O stretching vibrations, which are associated with the bond vibration of hydroxyl groups, alcohols, and ethers. The peak observed

Table 4 – Elemental analysis of the samples.

Sample	Percentage content (%)								
	C	O	Si	N	K	S	Al	Na	P
SAP	44.12	39.15	1.81	–	2.07	0.86	2.04	8.51	1.46
SAPC	44.56	38.95	–	–	1.12	0.26	–	–	0.40
R9	85.5	12.04	2.45	–	–	–	–	–	–
R11	83.05	10.66	0.87	5.42	–	–	–	–	–

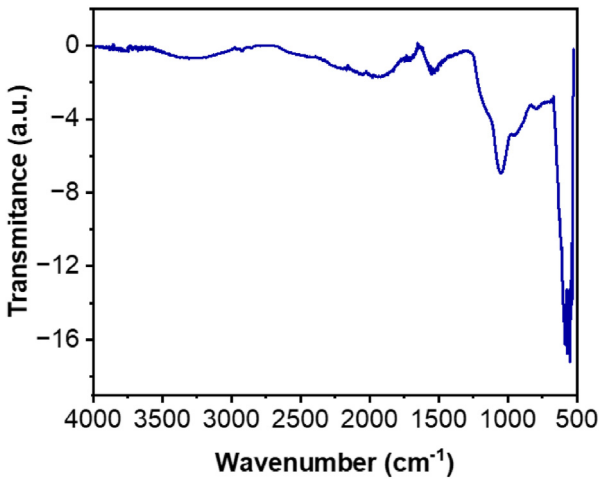

Fig. 4 – FTIR analysis of the R9 sample.

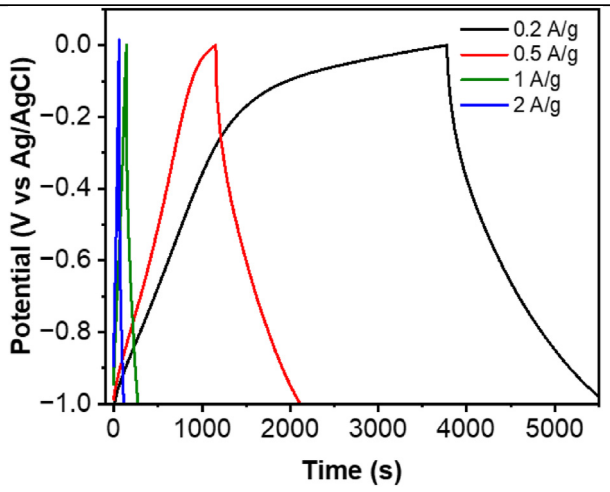

Fig. 5 – GCD curves of the R9 sample at different current densities.

around 1600 cm^{-1} is attributed to C=C stretching due to conjugation. The band at 750 cm^{-1} is assigned to C–H out-of-plane vibration, specifically related to benzene derivatives, confirming the aromatic nature of the activated carbon. The peak around 600 cm^{-1} is a result of O–H out-of-plane vibration [24]. Thesignal detected at ~3500 cm^{-1} indicates the presence of hydroxyl (O – H) bonds or N – H group on the carbon surface, which is common functional group for activated carbon materials [43,44].

3.5. *Galvanostatic charge-discharge analysis*

The energy storage performance of activated carbon electrodes was assessed through galvanostatic charge-discharge (GCD) tests conducted at various specific currents ranging from 0.2 A/g to 2 A/g. Fig. 5 displays the GCD curves at different specific currents for the R9 electrode sample. Notably, all the GCD curves exhibit a linear behavior, suggesting that the potential drop due to solution resistance is minimal and does not significantly affect the results [45]. This observation also confirms that the electrode materials display excellent electrical double-layer capacitive (EDLC) behavior, which is the predominant energy storage mechanism. The symmetry of these curves indicates good reversibility during the GCD process. Furthermore, it is evident that as the current density decreases, the charge and discharge times become longer. These times are directly proportional to the current densities. For instance, at 0.2 A/g, a complete cycle takes approximately 5500 s, while this cycle time decreases to 2250 s when the current density is increased to 0.5 A/g. It is worth highlighting that one of the targets set by the U.S. Department of Energy (DOE) is to achieve charging/discharging times between 3 and 5 min, a goal that can be met with current densities of 1 and 2 A/g.

3.6. *Cyclic voltammetry analysis*

The cyclic voltammetry (CV) curves for the R9 electrode made from SAP-activated carbon are depicted in Fig. 6a. The electrode has a surface area of 1 cm^2. A 6 M KOH electrolyte was utilized within a potential window spanning from −1 to 0 V, equating to a 1 V range. As outlined in Ref. [46], 6 M KOH is an exceptional electrolyte choice for carbon-based electrode materials, owing to its high concentration, which facilitates high hydrogen uptake. Additionally, the use of an alkaline electrolyte ensures that the reactions occur without Faradaic processes, contributing to stable behavior [47]. The CV

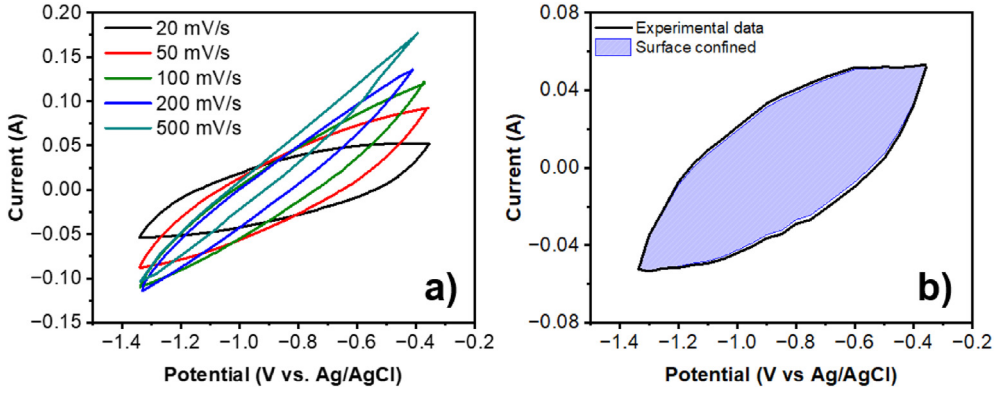

Fig. 6 – a) Cyclic voltammetry of the R9 samples at different voltage scan rates. b) Deconvoluted contribution of surface confined processes at 20 mV/s.

Table 5 – Specific capacity of the activated carbon electrodes.

Samples (R)	Q (mAh/g)	Hc (wt%)	C (F/g)	H (wt%)
1	1640	6.08	316	5.75
2	1114	4.13	307	3.81
3	1796	6.65	340	6.30
4	1291	4.78	284	4.49
5	1637	6.06	303	5.75
6	1191	4.41	271	4.13
7	1531	5.67	293	5.37
8	1836	6.80	340	6.45
9	1878	6.96	345	6.60
10	1657	6.14	309	5.82
11	959	3.55	253	3.29
12	1116	4.13	264	3.86
13	1057	3.92	297	3.61
14	1200	4.45	277	4.16
15	1196	4.43	321	4.1

Table 6 – Effect of activation conditions on hydrogen storage capacity.

Sample	A: Temperature (°C)	B: Time (h)	C: KOH:SAPC (wt/wt)	H (wt%)
1	700	2	2.5	5.75
2	900	1	2.5	3.81
3	700	1.5	1	6.30
4	800	1.5	2.5	4.49
5	800	2	1	5.75
6	800	1	4	4.13
7	900	1.5	1	5.37
8	700	1.5	4	6.45
9	700	1	2.5	6.60
10	800	1	1	5.82
11	900	1.5	4	3.29
12	800	2	4	3.86
13	900	2	2.5	3.61
14	800	1.5	2.5	4.16
15	800	1.5	2.5	4.10

experiments were conducted at various scan rates, ranging from 20 mV/s to 500 mV/s.

At the lowest scan rates (20 mV/s), the CV curves exhibit a limited current range without distinct redox peaks, suggesting the formation of a robust electric double layer (EDL). This EDL formation facilitates the accumulation of charge around the surface of the activated carbon. The shapes of the curves at these low scan rates appear quasi-rectangular, which is in line with expectations for an electric double layer. As the scan rates increase, the CV curves become narrower, and the current range achieved also expands. The area enclosed within the CV curves can be utilized to calculate the specific capacitance, which represents the highest specific capacitance achievable [45]. At higher scan rates (200 mV/s and 500 mV/s), more prominent peaks and oval shapes become noticeable. These shapes may be attributed to hydrogen adsorption when water splitting occurs, leading to a decrease in electrical conductivity [48]. To determine the contribution of surface-confined processes that occur during energy storage, the methodology outlined in Refs. [49,50] was followed. The deconvolution of this contribution is presented in Fig. 6b, wherein it is evident that this contribution accounts for nearly the entire experimentally obtained current.

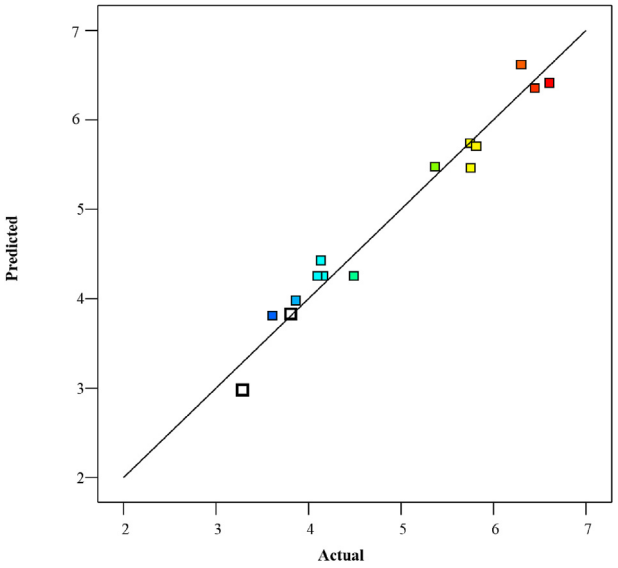

Fig. 7 – Predicted vs actual hydrogen storage capacity.

3.7. *Hydrogen uptake by the carbon electrode*

The results of the calculation of hydrogen storage capacity are summarized in Table 5. The charge (Q) in mAh/g was determined by integrating the discharge curves from the GCD test and integrating the area within the specific capacitance (C)

Table 7 – ANOVA analysis of the hydrogen storage capacity.

Source	Sum of Squares	df	Mean Square	F-value	*p*-value	
Model	17.25	5	3.45	31.53	<0.0001	**significant**
A-Activation Temperature	10.17	1	10.17	92.93	<0.0001	
C–KOH:SAPC	3.80	1	3.80	34.75	0.0002	
AC	1.24	1	1.24	11.35	0.0083	
A^2	1.20	1	1.20	10.97	0.0091	
C^2	0.9846	1	0.9846	9.00	0.0150	
Residual	0.9848	9	0.1094			
Lack of Fit	0.8968	7	0.1281	2.91	0.2793	**not significant**
Pure Error	0.0880	2	0.0440			
Cor Total	18.24	14				

Table 8 – Comparison of the performance of the best material presented in this work and other carbon materials reported for hydrogen adsorption.

Material	Precursor	Hydrogen storage capacity (wt%)	Reference
AC@MIL-101(Cr)	Fir bark & metallic organic framework	6.93	[53]
R9	Diaper waste	6.60	**This work**
P AC-KOH	Posidonia oceanica	6.4	[54]
PWAC-4	Peanut shell	6.36	[55]
S-2–800	Poplar sawdust	3.03	[56]
CNF/Co	Carbon nanofiber	2.70	[57]
AC-He400-N500	Commercial activated carbon	2.34	[58]
Ni decorated MWCNT	Ni & multi-walled carbon nanotubes	2.27	[59]
Pine tree bark activated carbon	Pine tree bark	1.39	[60]
AC-HIC	Coal fly ash	1.35	[61]
Lithium-loaded MWCNTs	Li & multi-walled carbon nanotubes	1.33	[62]

obtained from the CV curves. Based on this, the hydrogen sorption (HC) was calculated from the charge, and subsequently, the total hydrogen adsorbed for each sample was computed. Notably, all the tested electrodes exhibited a high storage capacity compared to many carbon-based materials used in this field, whether through cryogenic or electrochemical techniques. This enhanced performance can likely be attributed to the pore distribution and high specific surface area of the produced carbon. The lowest hydrogen storage capacity was observed for R11, with a charge of 953 mAh/g. In contrast, the highest capacity was recorded for the R9 sample, with a charge of 1640 mAh/g. The useable hydrogen capacity for the R9 sample is approximately 6.60 wt% H_2. Overall, around five of the electrode samples exhibit a gravimetric storage capacity surpassing the Department of Energy (DOE) standard of 5.6 kg H_2 for onboard vehicle applications.

An evaluation of the influence of activated carbon production conditions revealed that temperature and the KOH:SAPC molar ratio had the most significant impact on adsorption capacity (Table 6). Temperatures exceeding 800 °C did not favor the development of carbon characteristics conducive to higher hydrogen accumulation. Likewise, a higher KOH:SAPC ratio exceeding 2 wt% had an adverse effect on the properties of the activated carbon. BET analysis indicated a substantial reduction in surface area for the R11 sample, which was produced at 900 °C, 1.5 h, and with a KOH:SAPC ratio of 4. This reduction can be attributed in part to excessive KOH covering the surface of the SAPC particles, inhibiting the release of non-condensable gases. Additionally, high-temperature activation may result in increased burn-off and the transformation of micropores into macropores, consequently reducing the surface area [51,52].

The ANOVA analysis of the response surface model indicates that the obtained quadratic model is statistically significant, as evidenced by a *P*-value of <0.05 (Table 7). Moreover, the activation temperature, KOH:SAPC ratio, the interaction between activation temperature and KOH:SAPC molar ratio, the quadratic part of activation temperature, and KOH: SAPC ratio are all significant model terms with low *P*-values, signifying a 95% confidence level in the model. The R-squared value (R^2) obtained for this model is 0.9460, which is close to 1, indicating that the model adequately explains the variation in the experimental data. Model terms with *P*-values greater than 0.05 were considered non-significant and were omitted to create a more robust model with reduced model terms. The lack of fit value of 2.91 suggests that it is not statistically significant compared to pure error. The predicted versus actual hydrogen capacity plot (Fig. 7) demonstrates a close match between predictions and actual results, fitting well with the linear model. This indicates that the model can effectively guide the design process. The model equation in terms of coded factors with their coefficients is presented in Eq. (4).

$$H_2\ \text{capacity} = 4.32 - 1.13A - 0.6894C - 0.5573AC + 0.5684A^2 + 0.5149C^2 \quad (4)$$

Finally, by way of comparing the behavior of sample R9 with the results of other carbon-based materials previously published, Table 8 is presented, including the best hydrogen adsorption results achieved by these materials. As can be observed, sample R9 exhibits a hydrogen adsorption capacity comparable to the materials that show the best performance, thereby demonstrating the feasibility of using the precursor and activation method tested in this study.

4. Conclusions

The superabsorbent polymer (SAP) obtained from disposable diaper waste was utilized as an eco-friendly precursor for producing high microporous activated carbon. The Box-Behnken experimental design was employed to investigate the impact of activation conditions on textural, morphological, and hydrogen storage properties. Activation temperature and the ratio of potassium hydroxide (KOH) to carbonized SAPC were found to be critical factors influencing the carbon's textural characteristics, especially its ability to store hydrogen.

The most promising carbon exhibited impressive characteristics, including a surface area of 2552 m^2/g, total pore volume of 1.28 cm^3/g, total micropore volume of 0.871 cm^3/g, and a pore size of 1.32 nm. Electrodes constructed using this carbon material demonstrated exceptional hydrogen storage capacity, mainly attributable to the high surface area and dominant micropores. Galvanostatic charge/discharge (GCD) testing revealed that higher current densities of 1 and 2 A/g

enabled faster hydrogen discharge, meeting the Department of Energy (DOE) standard (3–5 min) when compared to lower current densities. However, elevated current densities had implications for electrode stability, processing time, and the quantity of stored hydrogen.

Cyclic voltammetry demonstrated that lower scan rates of 20 and 50 mV/s maintained a rectangular profile without observable redox peaks, indicating significant hydrogen storage. The primary mechanism for hydrogen storage was the electric double layer. Under the activation conditions of 700 °C, 1 h, and a KOH:SPAC ratio of 1, an exceptionally high specific capacity of 1878 mAh/g was achieved, corresponding to 6.60 wt% H_2. The developed model was statistically significant, robust, and can effectively guide the design process within the specified design space, as indicated by an R^2 value of 0.9460.

Declaration of competing interest

The authors declare that they have no known competing financial interests or personal relationships that could have appeared to influence the work reported in this paper.

Acknowledgment

The authors of this work gratefully acknowledge the technical support of R. Morán-Elvira for help with SEM and EDS analysis and R. Nava-Lara for FTIR analysis. This work was financially supported by Dirección General de Asuntos del Personal Académico, Mexico under Programa de Apoyo a Proyectos de Investigación e Innovación Tecnológica (DGAPA-PAPIIT) Project Nos: IA102522. César Giovanni-Mondragón received the CONAHCYT fellowship.

Appendix A. Supplementary data

Supplementary data to this article can be found online at https://doi.org/10.1016/j.ijhydene.2023.09.239.

REFERENCES

[1] Lobato-Peralta DR, Duque-Brito E, Villafán-Vidales HI, Longoria A, Sebastian PJ, Cuentas-Gallegos AK, et al. A review on trends in lignin extraction and valorization of lignocellulosic biomass for energy applications. J Clean Prod 2021;293. https://doi.org/10.1016/j.jclepro.2021.126123.

[2] Okoye PU, Mondragon CG, Okolie JA. Fuel storage application of activated carbon. In: Verma C, Quraishi MA, editors. Activated carbon: progress and applications. The Royal Society of Chemistry; 2023. p. 0. https://doi.org/10.1039/BK9781839169861-00179.

[3] Sedighi F, Ghiyasiyan-Arani M, Behpour M. Ternary nanocomposites of Ce2W2O9/CoWO4/porous carbon; design, structural study and electrochemical hydrogen storage application. Fuel 2022;310. https://doi.org/10.1016/j.fuel.2021.122218.

[4] Kaur M, Pal K. Potential electrochemical hydrogen storage in nickel and cobalt nanoparticles-induced zirconia-graphene nanocomposite. J Mater Sci Mater Electron 2020;31:10903–11. https://doi.org/10.1007/s10854-020-03641-y.

[5] Gholami T, Salavati-Niasari M, Salehabadi A, Amiri M, Shabani-Nooshabadi M, Rezaie M. Electrochemical hydrogen storage properties of NiAl2O4/NiO nanostructures using TiO2, SiO2 and graphene by auto-combustion method using green tea extract. Renew Energy 2018;115:199–207. https://doi.org/10.1016/j.renene.2017.08.037.

[6] Chibani A, Bougriou C. Effect of the tank geometry on the storage and destocking of hydrogen on metal hydride (LaNi5–H2). Int J Hydrogen Energy 2017;42:23035–44. https://doi.org/10.1016/j.ijhydene.2017.07.102.

[7] Ramezani Z, Dehghani H. Synthesis of strontium chromate-nitrogen and sulfur co-doped graphene and its potential for electrochemical hydrogen storage. Int J Hydrogen Energy 2022;47:1026–35. https://doi.org/10.1016/j.ijhydene.2021.10.057.

[8] Zhao H, Han M, Wang Y, Zhou Y, Ning Y, Jia H. Synthesis of prussian blue analogue derived porous Mo2C/Co9S8/N-doped carbon composite for electrochemical hydrogen storage application. Int J Hydrogen Energy 2023. https://doi.org/10.1016/j.ijhydene.2023.06.252.

[9] Shojaeinia A, Aghajani H, Tabrizi AT. Evaluation of electrochemical hydrogen storage capability of graphene oxide multi-layer coating. Int J Hydrogen Energy 2023;48:5836–49. https://doi.org/10.1016/j.ijhydene.2022.11.184.

[10] Simani M, Dehghani H. The study of electrochemical hydrogen storage behavior of the UiO-66 framework on the metal/reduced graphene oxide substrate. Fuel 2023;341. https://doi.org/10.1016/j.fuel.2023.127624.

[11] Abdi S, Mansournia M. A new approach to synthesize ammonium uranate decorated reduced graphene oxide nanosheets and their performance in electrochemical hydrogen storage. Fuel 2023;342. https://doi.org/10.1016/j.fuel.2023.127704.

[12] Andrews J, Ojha R, Rezaei Niya SM, Seibt S. Electrochemical storage reactions of hydrogen in activated carbon from phenolic resin. Catal Today 2022;397–399:155–64. https://doi.org/10.1016/j.cattod.2021.11.015.

[13] Liu X, Zhang C, Geng Z, Cai M. High-pressure hydrogen storage and optimizing fabrication of corncob-derived activated carbon. Microporous Mesoporous Mater 2014;194:60–5. https://doi.org/10.1016/j.micromeso.2014.04.005.

[14] Tellez-Juárez MC, Fierro V, Zhao W, Fernández-Huerta N, Izquierdo MT, Reguera E, et al. Hydrogen storage in activated carbons produced from coals of different ranks: effect of oxygen content. Int J Hydrogen Energy 2014;39:4996–5002. https://doi.org/10.1016/j.ijhydene.2014.01.071.

[15] Heo YJ, Park SJ. Synthesis of activated carbon derived from rice husks for improving hydrogen storage capacity. J Ind Eng Chem 2015;31:330–4. https://doi.org/10.1016/j.jiec.2015.07.006.

[16] Lu F, Wei C, Yin X, Kang L, Zhu M, Dai B. The effect of sp2 content in carbon on its catalytic activity for acetylene hydrochlorination. Nanomaterials 2022;12. https://doi.org/10.3390/nano12152619.

[17] Ye J, Ong MT, Heo TW, Campbell PG, Worsley MA, Liu Y, et al. Universal roles of hydrogen in electrochemical performance of graphene: high rate capacity and atomistic origins. Sci Rep 2015;5. https://doi.org/10.1038/srep16190.

[18] Radosinski L, Kuchta B. Hydrogen chemisorption on carbon structure with mixed sp2–sp3 hybridization: empirical potential studies. Adsorption 2014;20:875–82. https://doi.org/10.1007/s10450-014-9629-5.

[19] Oberoi AS, Nijhawan P, Singh P. A novel electrochemical hydrogen storage-based proton battery for renewable energy storage. Energies 2019;12. https://doi.org/10.3390/en12010082.
[20] Epelle EI, Desongu KS, Obande W, Adeleke AA, Ikubanni PP, Okolie JA, et al. A comprehensive review of hydrogen production and storage: a focus on the role of nanomaterials. Int J Hydrogen Energy 2022;47:20398–431. https://doi.org/10.1016/j.ijhydene.2022.04.227.
[21] Mohan M, Sharma VK, Kumar EA, Gayathri V. Hydrogen storage in carbon materials, vols. 1–26. Energy Storage-Wiley; 2019. https://doi.org/10.1002/est2.35.
[22] Bénard P, Chahine R. Carbon nanostructures for hydrogen storage. Solid-State Hydrogen Storage: Mater Chem 2008;261–87. https://doi.org/10.1533/9781845694944.3.261.
[23] Akbarzadeh R, Ghaedi M, Nasiri Kokhdan S, Vashaee D. Remarkably improved electrochemical hydrogen storage by multi-walled carbon nanotubes decorated with nanoporous bimetallic Fe-Ag/TiO 2 nanoparticles. Dalton Trans 2019;48:898–907. https://doi.org/10.1039/c8dt03897j.
[24] Hajialigol S, Masoum S. Promising electrochemical hydrogen storage properties of nano biomass derived from walnut shell. Int J Hydrogen Energy 2019;44:10713–21. https://doi.org/10.1016/j.ijhydene.2019.02.142.
[25] Dial C, Wahl G. Diaper industry workshop report. 1991.
[26] Lobato-Peralta DR, Arias DM, Okoye PU. Polymer superabsorbent from disposable diaper as a sustainable precursor for the development of stable supercapacitor electrode. J Energy Storage 2021;40. https://doi.org/10.1016/j.est.2021.102760.
[27] Colón J, Ruggieri L, Sánchez A, González A, Puig I. Possibilities of composting disposable diapers with municipal solid wastes. Waste Manag Res 2011;29:249–59. https://doi.org/10.1177/0734242X10364684.
[28] Zou J, Fan C, Jiang Y, Liu X, Zhou W, Xu H, et al. A preliminary study on assessing the Brunauer-Emmett-Teller analysis for disordered carbonaceous materials. Microporous Mesoporous Mater 2021;327:111411. https://doi.org/10.1016/J.MICROMESO.2021.111411.
[29] Fizer O, Fizer M, Filep M, Sidey V, Mariychuk R. On the structure of cetylpyridinium perchlorate: a combined XRD, NMR, IR and DFT study. J Mol Liq 2022;368:120659. https://doi.org/10.1016/J.MOLLIQ.2022.120659.
[30] Licht F, Davis MA, Andreas HA. Charge redistribution and electrode history impact galvanostatic charging/discharging and associated figures of merit. J Power Sources 2020;446:227354. https://doi.org/10.1016/J.JPOWSOUR.2019.227354.
[31] Lobato-Peralta DR, Duque-Brito E, Orugba HO, Arias DM, Cuentas-Gallegos AK, Okolie JA, et al. Sponge-like nanoporous activated carbon from corn husk as a sustainable and highly stable supercapacitor electrode for energy storage. Diam Relat Mater 2023;138:110176. https://doi.org/10.1016/j.diamond.2023.110176.
[32] Fuller TF, Harb JN. Electrochemical engineering. 2018.
[33] Aderyani S, Flouda P, Shah SA, Green MJ, Lutkenhaus JL, Ardebili H. Simulation of cyclic voltammetry in structural supercapacitors with pseudocapacitance behavior. Electrochim Acta 2021;390:138822. https://doi.org/10.1016/J.ELECTACTA.2021.138822.
[34] Babel K, Janasiak D, Jurewicz K. Electrochemical hydrogen storage in activated carbons with different pore structures derived from certain lignocellulose materials. Carbon N Y 2012;50:5017–26. https://doi.org/10.1016/j.carbon.2012.06.030.
[35] Thommes M, Kaneko K, Neimark AV, Olivier JP, Rodriguez-Reinoso F, Rouquerol J, et al. Physisorption of gases, with special reference to the evaluation of surface area and pore size distribution (IUPAC Technical Report). Pure Appl Chem 2015;87:1051–69. https://doi.org/10.1515/pac-2014-1117.
[36] Lobato-Peralta DR, Ayala-Cortés A, Longoria A, Pacheco-Catalán DE, Okoye PU, Villafán-Vidales HI, et al. Activated carbons obtained by environmentally friendly activation using solar energy for their use in neutral electrolyte supercapacitors. J Energy Storage 2022;52. https://doi.org/10.1016/j.est.2022.104888.
[37] Doğan M, Sabaz P, Bicil Z, Koçer Kizilduman B, Turhan Y. Activated carbon synthesis from tangerine peel and its use in hydrogen storage. J Energy Inst 2020. https://doi.org/10.1016/j.joei.2020.05.011.
[38] Chen YC, Lin LY. Investigating the redox behavior of activated carbon supercapacitors with hydroquinone and p-phenylenediamine dual redox additives in the electrolyte. J Colloid Interface Sci 2019;537:295–305. https://doi.org/10.1016/J.JCIS.2018.11.026.
[39] Jothi Ramalingam R, Sivachidambaram M, Vijaya JJ, Al-Lohedan HA, Muthumareeswaran MR. Synthesis of porous activated carbon powder formation from fruit peel and cow dung waste for modified electrode fabrication and application. Biomass Bioenergy 2020;142:105800. https://doi.org/10.1016/j.biombioe.2020.105800.
[40] Manasa P, Lei ZJ, Ran F. Biomass waste derived low cost activated carbon from carchorus olitorius (Jute Fiber) as sustainable and novel electrode material. J Energy Storage 2020;30. https://doi.org/10.1016/j.est.2020.101494.
[41] Ortiz-Olivares RD, Lobato-Peralta DR, Arias DM, Okolie JA, Cuentas-Gallegos AK, Sebastian PJ, et al. Production of nanoarchitectonics corncob activated carbon as electrode material for enhanced supercapacitor performance. J Energy Storage 2022;55. https://doi.org/10.1016/j.est.2022.105447.
[42] Solgi M, Najib T, Ahmadnejad S, Nasernejad B. Synthesis and characterization of novel activated carbon from Medlar seed for chromium removal: experimental analysis and modeling with artificial neural network and support vector regression. Resource-Effi Technol 2017;3:236–48. https://doi.org/10.1016/J.REFFIT.2017.08.003.
[43] Zhang L, Dong Y, Zhang D, Li W, Qin H, Luo Z, et al. Facile preparation of nitrogen-doped microporous carbon from potassium citrate/urea for effective CH4 separation and uptake. Fuel 2023;351. https://doi.org/10.1016/j.fuel.2023.128915.
[44] Wang J, Li X, Guo W, Tian K, Zhang J, Zhang B, et al. Activation-induced bowl-shaped nitrogen and oxygen dual-doped carbon material and its excellent supercapacitance. J Mater Sci Technol 2023;160:1–8. https://doi.org/10.1016/j.jmst.2023.03.018.
[45] Ali GAM, Sadegh H, Yusoff MM, Chong KF. Highly stable symmetric supercapacitor from cysteamine functionalized multi-walled carbon nanotubes operating in a wide potential window. Mater Today Proc 2019;16:2273–9. https://doi.org/10.1016/J.MATPR.2019.06.121.
[46] Barzegar F, Momodu DY, Fashedemi OO, Bello A, Dangbegnon JK, Manyala N. Investigation of different aqueous electrolytes on the electrochemical performance of activated carbon-based supercapacitors. RSC Adv 2015;5:107482–7. https://doi.org/10.1039/C5RA21962K.
[47] Silva LSV, Mansani GL, Yoshikawa DS, Casini JCS, Faria RN. Influence of the electrolyte potential window on the electrical characteristics of supercapacitors operating elevated temperatures. Mater Sci Forum 2020;1012:147–52. https://doi.org/10.4028/WWW.SCIENTIFIC.NET/MSF.1012.147.
[48] Park HY, Lee CH, Cho DW, Lee CH, Park JH. Synthesis of porous carbon derived from poly(vinylidenefluoride) and its

adsorption characteristics for CO2 and CH4. Microporous Mesoporous Mater 2020;299:110121. https://doi.org/10.1016/j.micromeso.2020.110121.

[49] Shi W, Hu B, Zhang H, Li J, Yang J, Liu J. Carbon-encapsulated iron oxide nanoparticles in self-supporting carbon nanofiber for high-performance supercapacitor in acid electrolyte with superior stability. ACS Appl Energy Mater 2020;3:12652–61. https://doi.org/10.1021/acsaem.0c02571.

[50] Seyed-Talebi SM, Cheraghizade M, Beheshtian J, Kuan CH, Diau EWG. Electrodeposition of CoxNiVyOz ternary nanopetals on bare and rGO-coated nickel foam for high-performance supercapacitor application. Nanomaterials 2022;12. https://doi.org/10.3390/nano12111894.

[51] Hu M, Ye Z, Zhang Q, Xue Q, Li Z, Wang J, et al. Towards understanding the chemical reactions between KOH and oxygen-containing groups during KOH-catalyzed pyrolysis of biomass. Energy 2022;245. https://doi.org/10.1016/j.energy.2022.123286.

[52] Yang HM, Zhang DH, Chen Y, Ran MJ, Gu JC. Study on the application of KOH to produce activated carbon to realize the utilization of distiller's grains. IOP conf ser earth environ sci, vol. 69. Institute of Physics Publishing; 2017. https://doi.org/10.1088/1755-1315/69/1/012051.

[53] Luo L, Zhou Y, Yan W, Luo L, Deng J, Fan M, et al. In-situ one-step synthesis of activated Carbon@MIL-101 (Cr) composites for hydrogen storage. Int J Hydrogen Energy 2022;47:39563–71. https://doi.org/10.1016/j.ijhydene.2022.09.128.

[54] Pedicini R, Maisano S, Chiodo V, Conte G, Policicchio A, Agostino RG. Posidonia Oceanica and Wood chips activated carbon as interesting materials for hydrogen storage. Int J Hydrogen Energy 2020;45:14038–47. https://doi.org/10.1016/j.ijhydene.2020.03.130.

[55] Li X, Tian H, Yan S, Shi H, Wu J, Sun Y, et al. Micropores enriched ultra-high specific surface area activated carbon derived from waste peanut shells boosting performance of hydrogen storage. Int J Hydrogen Energy 2023. https://doi.org/10.1016/j.ijhydene.2023.07.094.

[56] Liang Y, Wang Y, Ding N, Liang L, Zhao S, Yin D, et al. Preparation and hydrogen storage performance of poplar sawdust biochar with high specific surface area. Ind Crops Prod 2023;200. https://doi.org/10.1016/j.indcrop.2023.116788.

[57] Chang C, Gao P, Bao D, Wang L, Wang Y, Chen Y, et al. Ball-milling preparation of one-dimensional Co-carbon nanotube and Co-carbon nanofiber core/shell nanocomposites with high electrochemical hydrogen storage ability. J Power Sources 2014;255:318–24. https://doi.org/10.1016/j.jpowsour.2014.01.034.

[58] Morandé A, Lillo P, Blanco E, Pazo C, Dongil AB, Zarate X, et al. Modification of a commercial activated carbon with nitrogen and boron: hydrogen storage application. J Energy Storage 2023;64. https://doi.org/10.1016/j.est.2023.107193.

[59] Rather SU, Nahm KS. Hydrogen uptake of high-energy ball milled nickel-multiwalled carbon nanotube composites. Mater Res Bull 2014;49:525–30. https://doi.org/10.1016/j.materresbull.2013.09.022.

[60] Çetingürbüz E, Turkyilmaz A. Production of activated carbon by lithium activation and determination of hydrogen storage capacity. Ind Crops Prod 2023;203. https://doi.org/10.1016/j.indcrop.2023.117171.

[61] Musyoka NM, Wdowin M, Rambau KM, Franus W, Panek R, Madej J, et al. Synthesis of activated carbon from high-carbon coal fly ash and its hydrogen storage application. Renew Energy 2020;155:1264–71. https://doi.org/10.1016/j.renene.2020.04.003.

[62] Aghababaei M, Ghoreyshi AA, Esfandiari K. Optimizing the conditions of multi-walled carbon nanotubes surface activation and loading metal nanoparticles for enhanced hydrogen storage. Int J Hydrogen Energy 2020;45:23112–21. https://doi.org/10.1016/j.ijhydene.2020.06.201.